



<b>Publication Year</b>	2022
<b>Acceptance in OA</b>	2023-01-19T15:17:46Z
<b>Title</b>	A fully-analytical treatment of stray light in silicon pore optics for the ATHENA X-ray telescope
<b>Authors</b>	SPIGA, Daniele, SIRONI, GIORGIA, Della Monica Ferreira, D., Bavdaz, M., Bergbäck Knudsen, E., Ferreira, I., Jegers, A. S., MORETTI, Alberto
<b>Publisher's version (DOI)</b>	10.1117/12.2622220
<b>Handle</b>	<a href="http://hdl.handle.net/20.500.12386/32938">http://hdl.handle.net/20.500.12386/32938</a>
<b>Serie</b>	PROCEEDINGS OF SPIE
<b>Volume</b>	12181

# A fully-analytical treatment of stray light in silicon pore optics for the ATHENA X-ray telescope

D. Spiga,<sup>1</sup> G. Sironi,<sup>1</sup> D. Della Monica Ferreira,<sup>2</sup> M. Bavdaz,<sup>3</sup> E. Bergbäck Knudsen,<sup>4</sup>  
I. Ferreira,<sup>3</sup> A. S Jegers,<sup>2</sup> A. Moretti,<sup>1</sup>

<sup>1</sup>INAF – Brera Astronomical Observatory, Via Bianchi 46, 23807, Merate (Italy)

<sup>2</sup>DTU Space, Techn. Univ. of Denmark, Elektrovej, bygn. 327, 2800 Kgs. Lyngby (Denmark)

<sup>3</sup>European Space Agency, ESTEC, Keplerlaan 1, 2201 AZ Noordwijk (The Netherlands)

<sup>4</sup>DTU Fysik, Techn. Univ. of Denmark, Fysikvej, bygn. 311, 2800 Kgs. Lyngby (Denmark)

## ABSTRACT

Just like in any other X-ray telescope, stray light is expected to be a potential issue for the ATHENA X-ray telescope, with a significant impact on the scientific goals. The most prominent cause of stray light in Wolter-I type optics is represented by rays that did not undergo double reflection and were reflected only singly, on either the parabolic or the hyperbolic segment. A minor contribution may, additionally, arise from the diffuse reflections on the backside of the pore membrane and ribs. Aiming at determining whether the resulting background is tolerable or not, the effective area for stray light has to be calculated. While ray-tracing is a standard and well-assessed tool to perform this task, it usually takes a considerable amount of computation time to trace a number of rays sufficient to reach an appropriate statistical significance, because only a minority of stray rays emerge unobstructed from the mirror assembly. In contrast, approaching the stray light from the analytical viewpoint takes several upsides: it is faster than ray-tracing, does not suffer from any statistical uncertainties, and allows one to better understand the role of the parameters at play. The only approximation involved is the double cone geometry, which however is largely applicable to ATHENA as far as the sole effective area is concerned. In this paper, we show how the analytical approach can be successfully adopted to model the stray light effective area in the ATHENA mirror assembly, as a function of the X-ray energy and of the source off-axis angle.

**Keywords:** ATHENA, silicon pore optics, stray light, analytical, effective area

## 1. INTRODUCTION

The Advanced Telescope for High-ENergy Astrophysics ATHENA, the second L-class mission selected by ESA within the Cosmic Vision Program with launch scheduled in the 2030's, is in progress of realization.<sup>1</sup> It will be the largest X-ray telescope ever built, with a 2.5 m diameter optical mirror module assembly, a 1.4 m<sup>2</sup> effective area at 1 keV, and an angular resolution of 5 arcsec half-energy width (HEW). The optical assembly of ATHENA currently foresees 600 mirror modules (MMs) with focal length  $f = 12$  m, based on the silicon pore optic (SPO) technology, which will be manufactured in series by the *cosine* company (Sassenheim, Netherlands).<sup>2</sup> SPO mirror modules are based on stacked, double-side polished, diced (to a width  $W$  and a length  $L$ ), monocrystalline silicon wafers, in which grooves with rectangular sections are carved in the tangential direction in order to enable the propagation of X-rays. One polished surface, untouched by the etching process, is used to reflect X-rays with minimal scattering effects; the focusing curvature is achieved by stacking the plates on a mandrel that makes them reproduce the shape of a focusing element with a sagittal (azimuthal) curvature radius,  $R_0$ , equal to the distance from the optical axis. The structures remaining in the wafer thickness (*ribs*, oriented radially with azimuthal thickness  $t$ , and *membranes*, oriented azimuthally with radial thickness  $\tau$ ) play an important role in ensuring the stiffness of the stack and to maintain the expected angular resolution, at the same time keeping the mass-to-area ratio as low as possible. One stack with parabolic tangential (longitudinal) profile and one with hyperbolic tangential profile constitute an X-ray optical unit (XOU) and reconstruct in each pore the geometry of a Wolter-I mirror<sup>3</sup> via two reflections in sequence. An MM is made of two XOUs operating in parallel (Fig. 1). Due to the very low  $L/f$  ratio, the tangential profile does not strictly need to be a parabola-hyperbola sequence

---

e-mail: [daniele.spiga@inaf.it](mailto:daniele.spiga@inaf.it), phone: +39-02-72320427

in order to fulfill HEW requirement: other possibilities include uniform curvature profiles, or a conical profile followed by a doubled uniform curvature.<sup>4</sup> For generality, we dub with "primary" and "secondary" the two reflecting surfaces of the Wolter-I profile (instead of "parabolic" or "hyperbolic"), from this point on.

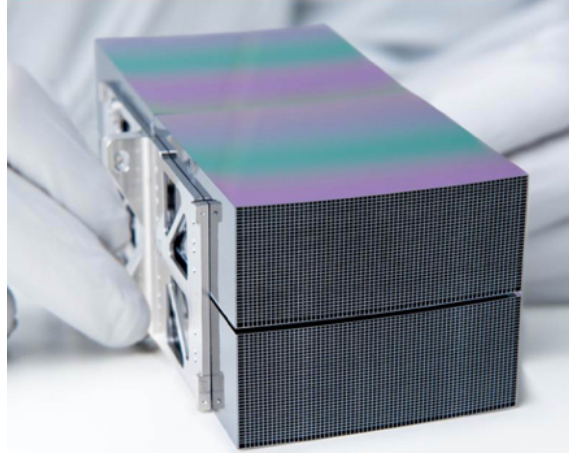


Figure 1. An SPO mirror module (image credits: ESA) consisting of two Wolter-I double stacks with 38 plate pairs each. A typical pore pitch is 2.3 mm, while the current pore height is 665  $\mu\text{m}$ . The mirror membrane is 170  $\mu\text{m}$  thick. The rib width can be either constant (also 170  $\mu\text{m}$  thick) or increasing toward the edges, for the inner mirror modules, in order to ease the rib alignment in the radial direction when the plates are bent.

Both primary and secondary plates are wedged in order to make  $2\alpha_0$ , the kink angle at the primary-secondary intersection plane (IP), increase with  $R_0$ , so as to preserve the sagittal focusing condition  $R_0 = f \tan(4\alpha_0)$ . This condition entails an increment of the  $\alpha_0$  angle by  $\Delta\alpha = (h + \tau)/4f$ . If  $\Delta\alpha$  is equal to the increment in the incidence angle on the primary plates, the condition on the kink angle entails an increment of  $3\Delta\alpha$  on the secondary plates. This wedge configuration is called +1/+3 and clearly requires manufacturing plates with two different wedges, and assembling two different kinds of stacks. Such a complication in the manufacturing process can be avoided adopting the same wedge in both SPO stacks, with the secondary one turned upside-down with respect to the primary (Fig. 2): in this case also, the angle between the primary and the secondary surface increases by  $2\Delta\alpha$  at every plate pair, ensuring the plate co-focality. The only price to pay for this simplification is a small loss of effective area, because all the plates – but the central one of each XOUs – see the source off-axis at increasing steps of  $2\Delta\alpha$ . This wedge configuration is called -1/+1 and currently represents the baseline for ATHENA:<sup>5</sup> however, a 0/+2 configuration is being considered also.

After the plate stacking, the primary and secondary stack are aligned, forming the correct kink angle, at the Physikalisch-Technische Bundesanstalt (PTB) laboratory of the BESSY-II synchrotron facility in Berlin.<sup>6</sup> In each XOUs, a small gap ( $\sim 1$  mm) between stacks remains and increases linearly from the innermost plate outwards, because all the plates in each stack have the same dimensions. The MMs will be systematically tested at the BEaTriX X-ray facility<sup>7</sup> in effective area (EA) and point spread function (PSF) performance, to be later aligned co-focally in the a mirror assembly (MA) at the UV optical bench at Medialario (Bosisio Parini, Italy).<sup>8</sup> While each XOUs has a Wolter-I configuration, the MA has a Wolter-Schwarzschild (WS) configuration,<sup>9</sup> in which the module centers form a spherical surface of radius  $f$ .

Just like any other geometry for X-ray optics, SPOs are affected by *stray light*. This encompasses rays that, rather than having two reflections in sequence on the polished surfaces, just make a single reflection (or an extra reflection on a pore backside or a wall, which are minimally reflective anyway). X-ray optics are in general designed to optimize the reflection for on-axis rays, coming from an infinitely distant source. However, when a source is off-axis by an angle  $\theta$ , or located at a finite distance  $S$ , some rays reflected by the primary can miss the reflection on the secondary plate. Other rays can skip the first reflection and hit the secondary mirror only. Most of these misplaced rays will hit the structures and be absorbed very likely. Others will reach the focal plane out of the detector area, and only a small fraction of them will eventually get to the detector area. However, if an intense X-ray source is just out of the telescope's field of view, there is some chance for the stray light to contaminate

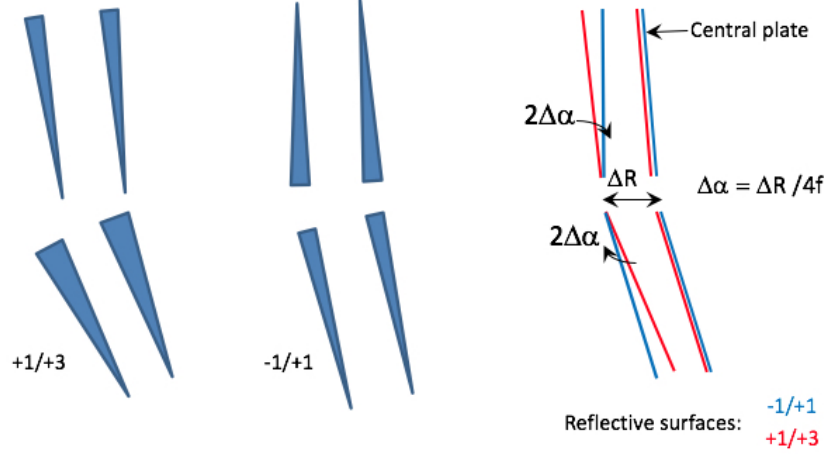


Figure 2. Different species of wedge configurations in SPOs. Left: +1/+3 configuration. Center: -1/+1 configuration, much simpler to manufacture. Right: in the -1/+1 configuration, the two surfaces form the correct mutual angle, even if the outer pair is tilted by  $2\Delta\alpha$  with respect to the +1/+3 one.

the detector field and so irremediably hamper the observation of faint objects. For this reason, assessing the sensitivity of an X-ray optic to stray light, i.e., its effective area as a function of  $\theta$  and the X-ray wavelength,  $\lambda$ , is a fundamental step in the design of an X-ray optical module. Should the EA of stray light seriously limit the sensitivity of an X-ray telescope, a pre-collimator (or baffle) can be adopted as a countermeasure to stop most stray light, without obstructing the focused flux, as it was done, e.g., for eROSITA.<sup>10</sup> For ATHENA, the dense obstruction of ribs will certainly help mitigate this issue, but since ATHENA was designed to be the most sensitive X-ray telescope ever, stray light cannot certainly be neglected *a priori*.

The stray light impact is usually assessed via dedicated ray-tracing routines.<sup>11</sup> For ATHENA, a very detailed assessment was done in the previous years by Willingale;<sup>12</sup> it turned out that the scientific performances of ATHENA would certainly benefit from a precollimator made of plate extension or grids: on the other hand, such grids should be mounted precisely aligned to the structures at the MA entrance. Any misalignments occurring, e.g., at the launch, even a few tens of microns between the pores and the grid structures, would cause a dramatic obstruction of the focused effective area of the telescope. Therefore, a precollimator for ATHENA is not foreseen in the design, as of today. Nonetheless, it can be useful to approach the stray light computation from an analytical point of view also, i.e., to find an expression for the stray light effective area  $A_{\text{pore}}(\lambda, \theta, \varphi)$  out of a single pore in an SPO MM, as described by its geometric parameters (Fig. 3) and its reflectivity,  $r_\lambda(\alpha)$ . The stray light contamination will thereby follow from the summation of the unobstructed areas of either primary or secondary surfaces (respectively named "primary stray light" (SL1) and "secondary stray light" (SL2)), as out the pores that reflect into the detector area. Finding this expression is the subject of this paper.

The analytical treatment of the effective area of a grazing-incidence mirror had been already provided and validated in previous papers; first for an integral double-reflection mirror,<sup>13</sup> then in the presence of nesting in an optical module,<sup>14</sup> and finally extended the stray light, accounting for all possible sources of obstruction.<sup>15, 16</sup> In the context of the "Silicon Pore Optics SIMulation and Modelling" (SiMPOSIUM) ESA-led project, we have extended the analytical approach to pore optics,<sup>17</sup> providing useful formulae for the focused effective area of a single pore in double reflection (2R), which also accounted for the azimuthal vignetting from ribs. In a subsequent step,<sup>18</sup> we have extended the effective area expression to the -1/+1 wedge configuration of plates. In all the previous contributions, as far as the effective area was concerned, the pore surfaces was modeled as a double cone profile to a very good approximation. Also in the ATHENA case we are allowed to do so, because the plate length,  $L$ , is much smaller than the focal length,  $f$ . Since the effective area estimate error – when approximating the Wolter-I with a double cone – is proportional to the ratio  $L/f$ ,<sup>13</sup> which in the SPO case boils down to a few percents, we adopt the double-cone approximation throughout this paper. In Sect. 2, we review the vignetting parameters and the vignetting coefficients involved in the 2R obstruction of light focused in a

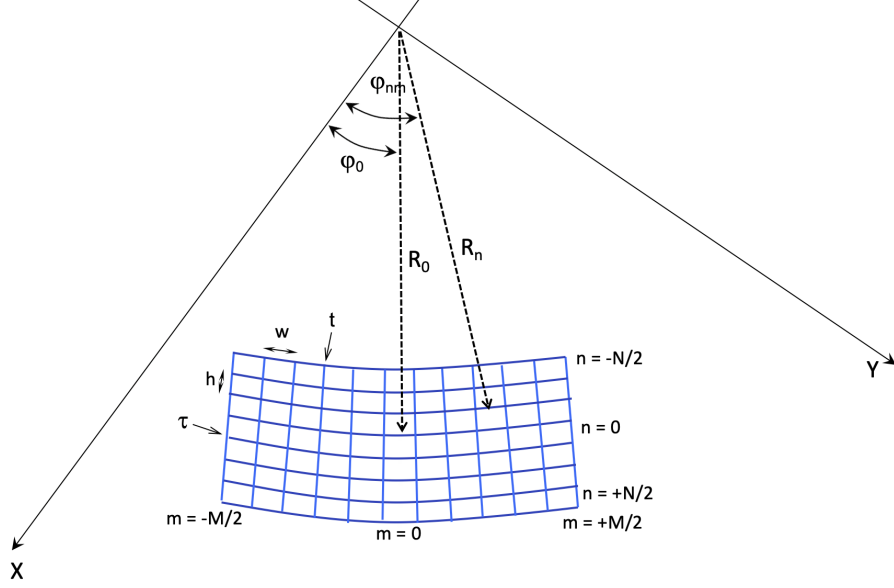


Figure 3. Schematic of the front view in an SPO mirror module. Pores are numbered via the integers  $(n, m)$  from the central one, located by the indices  $(0, 0)$ . The central pore is identified via the polar coordinates  $(R_0, \varphi_0)$ , and the generic pore in the module by  $(R_n, \varphi_{nm})$ . Due to the small pore size, the incidence angles in either reflection are approximately constant in each pore, and thereby depend only on the coordinates of the pore center.

densely nested structure, such as the one of SPOs. In Sect. 3, we show the extension of the formalism to a pore in an SPO, analyzing separately the contribution to SL1 (Sect. 3.1) and SL2 (Sect. 3.2). With respect to the previous papers, we also generalize the vignetting coefficients to plate pairs having the primary-secondary IPs axially scaled by  $\Delta z$  with respect to the inner one. Mathematical details, such as the general derivation of the vignetting coefficients modified to account for the  $\Delta z$  scaling, are deferred to appendix A: this generalization can be useful in view of possible future WS geometries within the MM structures. Some computation examples, showing the potentialities of the method, are provided in Sect. 4.

## 2. THE DOUBLE-REFLECTION EFFECTIVE AREA OF SILICON PORES

### 2.1 Incidence angles, vignetting parameters, and coefficients

We hereafter summarize the relevant results obtained throughout the previous papers. Step by step, we will progress in the construction of an equation for the effective area of the single pore, as a function of its structural parameters. The generic pore in a SPO mirror module can be identified via the polar coordinates  $(r, \varphi)$  in the chief plane of the ATHENA's optical assembly (see Fig. 3, where the polar coordinates take on discrete values,  $R_n$  and  $\varphi_{nm}$ ). The pore location is specified in the mirror module by two indices  $n, m$ . If we represent with  $(R_0, \varphi_0)$  the polar coordinates of the central pore at the intersection plane, and the  $nm$ -th pore is located at  $(R_n, \varphi_{nm})$ , then the other radii in the module are  $R_n = R_0 + n(h + \tau)$  and the polar angles are  $\varphi_{nm} = \varphi_0 + m\Delta\varphi_n$ , where  $\Delta\varphi_n = (w + t)/R_n$ . We initially assume a point-like source, located at distance  $S$ , located in the  $xz$  plane (i.e., at  $\varphi = 0$ ) and forming at a small angle  $\theta$  with the optical axis. Should the source be located out of the  $xz$  plane, say, at  $\varphi'$ , all the results can be immediately adapted, by just replacing  $\varphi_{nm} \rightarrow \varphi_{nm} - \varphi'$ .

The areas in an aperture that contribute to the double or the single reflections, usually crescent-shaped in integral mirror shells,<sup>14</sup> can be approximated by rectangles within a pore, due to its small size compared to  $R_0$ , as highlighted in Fig. 4. Some portions correspond to obstructed areas and get blocked, while unobstructed areas of double reflection contribute to the focused effective area, and to the stray light in single reflections. All the problem is therefore reduced to finding the dimensions of those rectangles (e.g., the red one for 2R and the green one for SL1 in Fig. 4), then multiplying their area by the surface reflectivity  $r_\lambda(\alpha)$  at the incidence angle  $\alpha$ . The relative dimensions of the rectangular areas are specified by the *vignetting coefficients*, expressing the

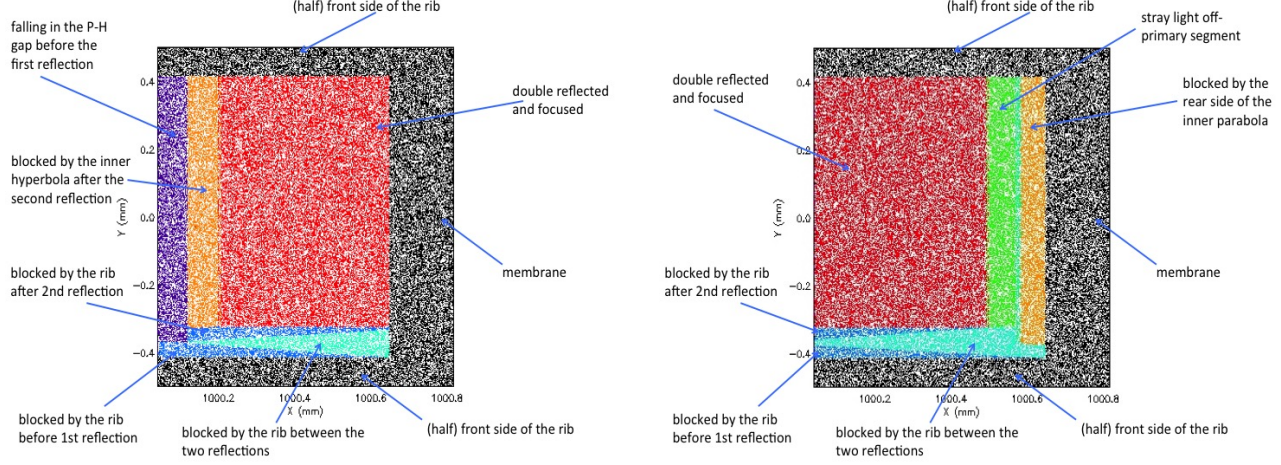


Figure 4. Entrance pupil of the same pore, for a source off-axis by  $\theta = 10$  arcmin and placed at (left)  $\varphi = 30$  deg, (right)  $\varphi = 150$  deg. The different colors refer to different possible destinies of the rays. Obstructions caused by the ribs occupy a rectangular region in the lower part of the figures, near the lateral wall of a rib. The reflectivity is assumed 100%.

unobstructed mirror length ratio, due to a specific source of obstruction.<sup>14</sup> We hereby summarize the relevant results, with some change of notation, and initially adopting the +1/+3 configuration.

1. We dub with  $\alpha_0^n$  the incidence angle for an on-axis source at infinity,  $2\alpha_0^n$  is the primary-secondary kink angle, and the relation  $R_n = f \tan 4\alpha_0^n$  holds. We denote the source divergence angle with  $\delta_n = R_n/S$ . If  $\theta$  is the off-axis angle, the incidence angles on the primary and the secondary mirror surface (Fig. 5, left) depend on of the polar angle  $\varphi_{nm}$  via the following equations:<sup>13</sup>

$$\alpha_1^{nm} = \alpha_0^n + \delta_n - \theta \cos \varphi_{nm}, \quad (1)$$

$$\alpha_2^{nm} = \alpha_0^n - \delta_n + \theta \cos \varphi_{nm}, \quad (2)$$

where the superscripts do *not* indicate powers of the angles. We note that  $\alpha_1^{nm} + \alpha_2^{nm} = 2\alpha_0^n$  and that the behavior of  $\alpha_1$  and  $\alpha_2$  is symmetric with respect to the  $x$ -axis. The expressions are valid if non-negative. For rays directly hitting the secondary plates, incidence occurs directly on a surface of slope  $3\alpha_0$  instead of  $\alpha_0$ , and the incidence angle  $\beta_2$  is given by

$$\beta_2^{nm} = 3\alpha_0^n + \delta_n - \theta \cos \varphi_{nm}. \quad (3)$$

We also introduce the  $\beta_1$  angle, defined as the incidence angle on the *rear* side of the primary segment of the same pair of plates, i.e.,  $\beta_1 = -\alpha_1$  (Eq. (1)).

2. The focused beam can be obstructed in three different ways. Obstruction occurs<sup>14</sup> when the incidence angles exceed three angles (see Fig. 5, right, for the explanation of symbols) that characterize the spacing left between the reflective and the obstructing pair, the *vignetting parameters*:

$$\Phi_n = \frac{R_0^n - R_M^{n*}}{L_1^{*n}} + \alpha_0^n, \quad \Psi_n = \frac{R_0^n - R_0^{n*}}{L_1^n}, \quad \Sigma_n = \frac{R_0^n - R_m^{n*}}{L_2^{n*}} - 3\alpha_0^n. \quad (4)$$

The plate lengths,  $L_1, L_2$ , and  $L_1^*, L_2^*$  are measured from the respective intersection planes and include the central gaps from the material plate end to the IP, i.e.,  $D_1, D_2$ , and  $D_1^*, D_2^*$ . The gaps are variable because the stacks are tilted for the central plates in each XOU to form the correct angles,  $\alpha_0^0$  and  $3\alpha_0^0$ , with the optical axis.

3. Only a fraction  $V$  of rays reflected by the primary surface of a pore impinges onto the secondary surface. Rays that miss the second reflection, if unobstructed, contribute to SL1 (Fig. 5, left). Analysis shows<sup>13</sup> that the  $V$  coefficient has the expression

$$V = \frac{L_2 \alpha_2}{L_1 \alpha_1}, \quad (5)$$



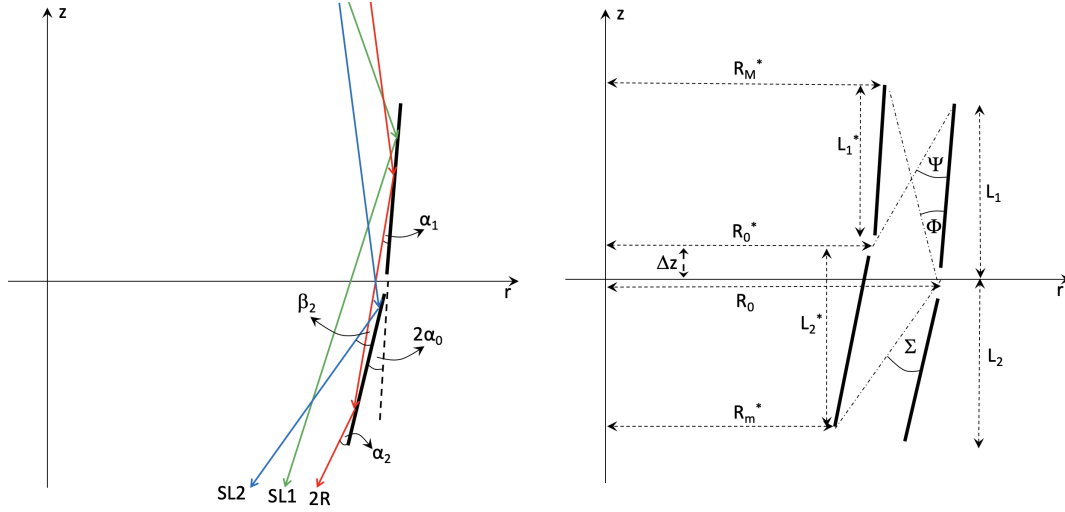


Figure 5. Left: Incidence angles on the primary and the secondary segment of a generic Wolter-I profile in radial section, for double reflection ( $\alpha_1$  and  $\alpha_2$ ) and for stray light ( $\alpha_1$  for stray light from the primary segment and  $\beta_2$  for direct incidence on the secondary one). Right: Radial section of a WS pair: geometrical meaning of the parameters, including  $\Phi$ ,  $\Psi$ , and  $\Sigma$ .  $\Delta z \geq 0$  is the axial distance between nearby IPs. The outer surface of the inner mirror acts as an obstructing element, and its parameters are marked with a \* superscript. The reflective surface of the outer mirror is on the right.

with the condition that  $0 \leq V \leq 1$ . The part of primary mirror that does not contribute to the double reflection is the always on the side of the mirror entrance.

- Due to three different ways the rays can be obstructed in (Fig. 6, left), only a fraction of the primary mirror length is effective at sending rays reflected twice to the focal plane. The unobstructed mirror length is expressed by the vignetting coefficients  $V_1$ ,  $V_2$ ,  $V_3$ , which are functions of  $\Phi$ ,  $\Psi$ ,  $\Sigma$  (Eq. (4)), and of  $\alpha_1$ ,  $\alpha_2$ . A detailed derivation was already provided for the Wolter-I configuration; for two plate pairs in WS geometry, the vignetting coefficients can be generalized as follows (appendix A.1):

$$V_1 = 1 + \frac{L_1^*(\Phi - \alpha_1) + \Delta z(\alpha_0 - \alpha_1)}{L_1 \alpha_1}, \quad (6)$$

$$V_2 = \frac{L_1 \Psi + \Delta z(\alpha_1 + \alpha_0)}{L_1 \alpha_1}, \quad (7)$$

$$V_3 = 1 + \frac{L_2^*(\Sigma - \alpha_2) + \Delta z(\alpha_2 + 3\alpha_0)}{L_1 \alpha_1}, \quad (8)$$

where we omitted the  $nm$  indices to simplify the notation. The coefficients are meant non-negative and not greater than 1. In Wolter-I configuration ( $\Delta z = 0$ ), the equations above correctly reduce to the usual expressions.<sup>14</sup>

- In addition to the previous species of vignetting that act in the tangential direction, SPO MMs are also affected by rib obstruction off-axis. We therefore introduce another vignetting coefficient, this time in the azimuthal direction, expressed by the formula

$$V_R = 1 - \frac{(L_1^n + L_2^n) \theta}{w} |\sin \varphi_{nm}|, \quad (9)$$

provided that it is non-negative and  $\geq 1$ , as usual. Equation (9) can immediately be derived<sup>19</sup> from an inspection of Fig. 6, right. Moreover, from Fig. 4 it becomes evident that this formula holds for stray light also (e.g., the green and the red rectangle have the same height). This is due to the negligible deviation in the  $\varphi$  coordinate between the two reflections.<sup>13</sup>

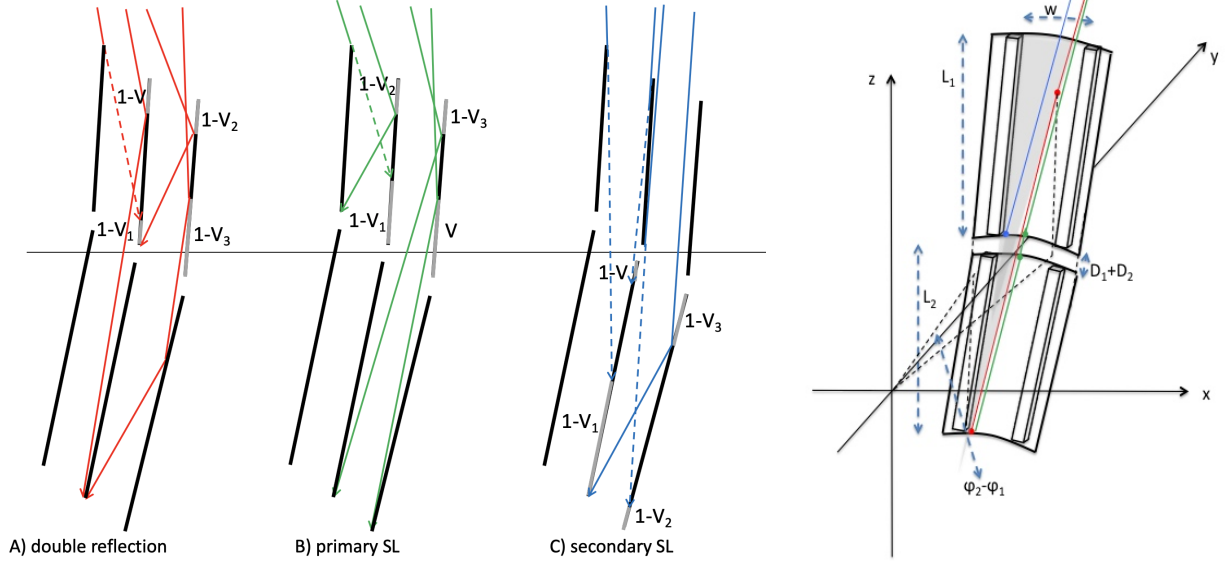


Figure 6. Left: all the possible tangential obstructions in an array of pores for A) double reflection, B) single reflection on the primary and C) on the secondary mirror. The unobstructed mirror length fraction is specified by the vignetting coefficients  $V$ ,  $V_1$ ,  $V_2$ ,  $V_3$ . Right: Off-axis obstruction by ribs. Obstructed ray before the first reflection (blue), after the first reflection (red), or after the second reflection (green). The deviation out of the incidence plane can be neglected.

6. Considering all the sources of vignetting above, and referring to Fig. 6A, we can easily derive the 2R effective area of a pore of angular amplitude  $\Delta\varphi_n = w/R_0^n$ , located at the polar angle  $\varphi_{nm}$ , for the moment neglecting the gaps between the primary and secondary stacks:

$$A_{2R}^{nm}(\lambda, \theta) = \underbrace{L_1^n \alpha_1^{nm} [\min(1, V, V_2) - \max(1 - V_1, 1 - V_3, 0)]}_{\text{tangential}} \underbrace{R_0^n V_R \Delta\varphi_n r_\lambda(\alpha_1^{nm}) r_\lambda(\alpha_2^{nm})}_{\text{azimuthal}}, \quad (10)$$

where  $r_\lambda(\alpha)$  is the coating reflectivity, and the two expressions above the brackets are nothing short of the two sides of the red rectangles in Fig. 4. To avoid negative contributions to the effective area, the expression enclosed in the  $[\ ]_{\geq 0}$  brackets has been zeroed when negative. For the same reason, we have added a "0" in the max operator. We finally consider that all the IPs in an MM coincide:  $\Delta z = 0$ . Substituting now Eqs. (5) through (9) into Eq. (10), we obtain the double-reflection effective area of the pore:

$$A_{2R}^{nm}(\lambda, \theta) = [\min(L_1 \alpha_1^{nm}, L_2 \alpha_2^{nm}, L_1 \Psi) - \max(L_1^*(\alpha_1^{nm} - \Phi), L_2^*(\alpha_2^{nm} - \Sigma), 0)]_{\geq 0} w V_R r_\lambda(\alpha_1^{nm}) r_\lambda(\alpha_2^{nm}), \quad (11)$$

which is valid on the usual condition that both incidence angles remain non-negative.

## 2.2 Primary-secondary gaps

We now extend the results, accounting for two small gaps  $D_1$  and  $D_2$  between the material end of the plates and the IP. The presence of the gaps reduces the effective area, because some rays can fall in the gap after the first reflection and so miss the second reflection. It can be shown<sup>19</sup> that the vignetting factor related to this effect is  $D_2 \alpha_2 / D_1 \alpha_1$ . We therefore have to remove from the effective area another term  $\max(D_1 \alpha_1, D_2 \alpha_2)$ , so that the "max" term in Eq. (11) turns into

$$\max(L_1^*(\alpha_1^{nm} - \Phi), L_2^*(\alpha_2^{nm} - \Sigma), D_1 \alpha_1^{nm}, D_2 \alpha_2^{nm}), \quad (12)$$

in which the "0" term is no longer needed. We now simplify Eq. (11) to derive a more compact expression for the effective area of the  $nm$ -th pore. We firstly consider that all the plates in an XOUI have the same material length  $L_1 - D_1$  and approximately covering, when projected perpendicular to the rays, the height of a pore, i.e.,  $(L_1 - D_1) \alpha_0^0 = h$ . Moreover, even if the gaps have a variable amplitude, due to the stack tilt by  $\alpha_0^0$  for the



primary and  $3\alpha_0^0$  for the secondary, the influence of such variation on the effective area is practically negligible. It can also be proven<sup>18</sup> that the slight change of the L's in a stack affects the effective area obstruction only marginally. We can so approximate the obstruction parameters with  $\Psi \simeq \alpha_0^0$  and  $\Phi \simeq \Sigma \simeq \alpha_0^0(1 - \xi_0)$ , after setting  $L_1 = L_2 = L_1^* = L_2^*$  equal to the central plate length  $L_0$ , and  $\xi_0 = D_0/L_0$ . We now return to Eq. (11), which we can rewrite as follows:

$$A_{2R}^{nm}(\lambda, \theta) \simeq wV_R L_0 [\min(\alpha_1^{nm}, \alpha_2^{nm}, \alpha_0^0) - \max(\alpha_1^{nm} - \Phi, \alpha_2^{nm} - \Phi, \xi_0 \alpha_1^{nm}, \xi_0 \alpha_2^{nm})]_{\geq 0} r_\lambda(\alpha_1^{nm}) r_\lambda(\alpha_2^{nm}). \quad (13)$$

Obviously, we are not forced to use Eq. (13), which is simplified with respect to the more exact form (Eqs. (11) through (12)). Nevertheless, Eq. (13) is suitable to a faster, although approximate, computation.

### 2.3 Accounting for the wedge configuration in SPOs for ATHENA

We now come to the expression of the incidence angles throughout the stack. In the +1/+3 configuration (Fig. 2, left), moving outwards, the on-axis incidence angle increases by steps  $\Delta\alpha_R = (h + \tau)/4f$  on both stacks, at every plate. This means  $\alpha_0^n = \alpha_0^0 + n\Delta\alpha_R$ , where the incidence angle of the central plate obeys the relation  $\alpha_0^0 = R_0/4f$ , which ensures the co-focality of all the MMs in the mirror assembly. In the -1/+1 configuration, the primary incidence angle should be *diminished* by  $2\Delta\alpha_R$  per layer, going outwards; the secondary incidence angle has to be increased by the same amount. So we can generally write the expressions for the incidence angles, assuming a source at infinity ( $\delta = 0$ ):

$$\alpha_1^{nm} = \alpha_0^n - 2n\Delta\alpha_w - \theta \cos \varphi_{nm}, \quad (14)$$

$$\alpha_2^{nm} = \alpha_0^n + 2n\Delta\alpha_w + \theta \cos \varphi_{nm}, \quad (15)$$

where the 2-nd terms play the role of a *negative* divergence, and where we have defined

$$\Delta\alpha_w = \begin{cases} 0 & \text{in +1/+3 wedge conf.,} \\ \Delta\alpha_R & \text{in -1/+1 wedge conf.,} \\ \Delta\alpha_R/2 & \text{in 0/+2 wedge conf.} \end{cases} \quad (16)$$

With the notation introduced above, we can compute the 2R effective area of the  $nm$ -th pore in an SPO MM using Eq. (13), with  $\Phi = \alpha_0^0(1 - \xi_0)$ , obviously taking a routine to calculate  $r_\lambda(\alpha)$  for granted. Supposing the gaps effect overwhelmed by the other sources of tangential obstruction, Eq. (13) can be written in an easier form:<sup>18</sup>

$$A_{2R}^{nm}(\lambda, \theta) \simeq [w - 2\theta L_0 |\sin \varphi_{nm}|]_{\geq 0} [h - 2L_0 |2n\Delta\alpha_w + \theta \cos \varphi_{nm}|]_{\geq 0} r_\lambda(\alpha_1^{nm}) r_\lambda(\alpha_2^{nm}), \quad (17)$$

where the  $\Delta\alpha_w$  parameter is given by Eq. (16). The total effective area of the ATHENA mirror assembly simply follows from summation over the  $nm$  indices.

## 3. THE STRAY LIGHT EFFECTIVE AREA IN SILICON PORES

### 3.1 Primary stray light

Once described the obstruction mechanisms in a pore optic, modeling stray light just requires a few changes in the vignetting coefficients. Three vignetting coefficients ( $V$ ,  $V_1$ ,  $V_2$ ) still describe obstructions of SL1 with the same expressions (Eqs. (5) through (7)) but, due to the different angles formed with the optical axis and the obstructing surfaces, the functional form of  $V_3$  differs from Eq. (8): for the reader interested in such details, we postpone the analytical derivation in appendix A.2. The resulting expression is:

$$V_3 = \frac{L_2^*(\Sigma + \alpha_2) + \Delta z(\alpha_1 + \alpha_0)}{L_1 \alpha_1}. \quad (18)$$

Clearly, no second reflection occurs, but we have anyway used the  $\alpha_2$  angle in Eq. (18) for notation convenience. This time, we do not require  $\alpha_2$  to be non-negative, and we can always carry the computation out by using the relation  $\alpha_1 + \alpha_2 = 2\alpha_0$ . Inspection of Fig. 6B shows that the effective area of a pore located at  $\varphi_{nm}$  must have

a form totally similar to Eq. (10), only changing the roles of the tangential vignetting coefficients.<sup>15</sup> The rib vignetting follows Eq. (9), even in single reflection.

$$A_{\text{SL1}}^{nm}(\lambda, \theta) = \underbrace{L_1^n \alpha_1^{nm} [\min(1, V_2, V_3) - \max(V, 1 - V_1, 0)]}_{\text{tangential}} \underbrace{\geq 0}_{\text{azimuthal}} \underbrace{R_0^n V_R \Delta \varphi_n}_{\text{azimuthal}} r_\lambda(\alpha_1^{nm}), \quad (19)$$

where, due to the single reflection, only the  $r_\lambda(\alpha_1)$  factor appears. Now substituting the expressions for the vignetting coefficients with  $\Delta z = 0$ , we easily obtain:

$$A_{\text{SL1}}^{nm}(\lambda, \theta) = [\min(L_1 \alpha_1^{nm}, L_1 \Psi, L_2^*(\Sigma + \alpha_2^{nm})) - \max(L_2 \alpha_2^{nm}, L_1^*(\alpha_1^{nm} - \Phi), 0)]_{\geq 0} w V_R r_\lambda(\alpha_1^{nm}), \quad (20)$$

provided that  $\alpha_1 \geq 0$ , but we also have to remove a radial element  $D_1 \alpha_1^{nm}$  as a possible contributor to the vignetting near the intersection plane (adding this to the "max" term also ensures that it remains non-negative). Setting all the plate lengths equal to  $L_0$  (including  $D_1$ ),  $\Phi \simeq \Sigma$ , and  $\Psi = \alpha_0^0$ , we have the simplified expression

$$A_{\text{SL1}}^{nm}(\lambda, \theta) \simeq L_0 [w - 2\theta L_0 |\sin \varphi_{nm}|]_{\geq 0} [\min(\alpha_1^{nm}, \alpha_0^0, \Phi + \alpha_2^{nm}) - \max(\alpha_2^{nm}, \alpha_1^{nm} - \Phi, \xi_0 \alpha_1^{nm})]_{\geq 0} r_\lambda(\alpha_1^{nm}). \quad (21)$$

Equation (21) enables the computation of the SL1 effective area of the  $nm$ -th pore, using the relation  $\Phi = \alpha_0^0(1 - \xi_0)$  and the definition of the incidence angles, Eqs. (14) and (15).

### 3.2 Secondary stray light

The treatment of secondary stray light follows guidelines similar to the ones used for SL1. Possible sources of obstruction in the meridional plane are depicted in Fig. 6C. Three of them ( $V$ ,  $V_1$ ,  $V_2$ ) occur before reflection, while  $V_3$  describes the vignetting after reflection. The functional form, however, utterly differs from those used in the previous sections. In WS configuration, this requires one to re-compute the coefficients (see appendix A.3), with the results:

$$V_1 = \frac{L_1^*(\Phi - \alpha_1) + \Delta z(\alpha_0 - \alpha_1)}{L_2 \beta_2}, \quad (22)$$

$$V_2 = \frac{L_1 \Psi + \Delta z(\alpha_0 - \alpha_1)}{L_2 \beta_2}, \quad (23)$$

$$V_3 = 1 + \frac{L_2^*(\Sigma - \beta_2) + \Delta z(\beta_2 + 3\alpha_0)}{L_2 \beta_2}. \quad (24)$$

We have used the angle  $\alpha_1$  for convenience of notation, but it is only a parameter involved in the obstruction, as there is no incidence on the primary mirror. Double reflection plays no role in this kind of stray light; hence, the usual  $V$  coefficient (Eq. 5)) cannot be used. There is, however, the shadow cast by the *reflective* primary segment onto its secondary one, and the non-obstructed fraction is, this time (see appendix A.3),

$$V = 1 - \frac{L_1 \beta_1}{L_2 \beta_2}. \quad (25)$$

where  $\beta_1 = -\alpha_1$ , and  $\beta_2$  is the angle of direct incidence on the secondary plates (Eq. (3)). We can therefore write, inspecting Fig. 6C, the effective area of the  $nm$ -th pore as:

$$A_{\text{SL2}}^{nm}(\lambda, \theta) = \underbrace{L_2^n \beta_2^{nm} [\min(1, V_1, V_2) - \max(1 - V, 1 - V_3, 0)]}_{\text{tangential}} \underbrace{\geq 0}_{\text{azimuthal}} \underbrace{R_0^n V_R \Delta \varphi_n}_{\text{azimuthal}} r_\lambda(\beta_2^{nm}), \quad (26)$$

which easily becomes, using the previous expressions with  $\Delta z = 0$ ,

$$A_{\text{SL2}}^{nm}(\lambda, \theta) = [\min(L_2 \beta_2^{nm}, L_1^*(\Phi - \alpha_1^{nm}), L_1 \Psi) - \max(L_1 \beta_1^{nm}, L_2^*(\beta_2^{nm} - \Sigma), 0)]_{\geq 0} w V_R r_\lambda(\beta_2^{nm}). \quad (27)$$

Now, removing an element  $D_2 \beta_2$  from the projected length, and setting all the plate lengths equal to a common value  $L_0$ , we obtain the simplified expression:

$$A_{\text{SL2}}^{nm}(\lambda, \theta) \simeq L_0 [w - 2\theta L_0 |\sin \varphi_{nm}|]_{\geq 0} [\min(\beta_2^{nm}, \Phi + \beta_1^{nm}, \alpha_0^0) - \max(\beta_1^{nm}, \beta_2^{nm} - \Phi, \xi_0 \beta_2^{nm})]_{\geq 0} r_\lambda(\beta_2^{nm}), \quad (28)$$

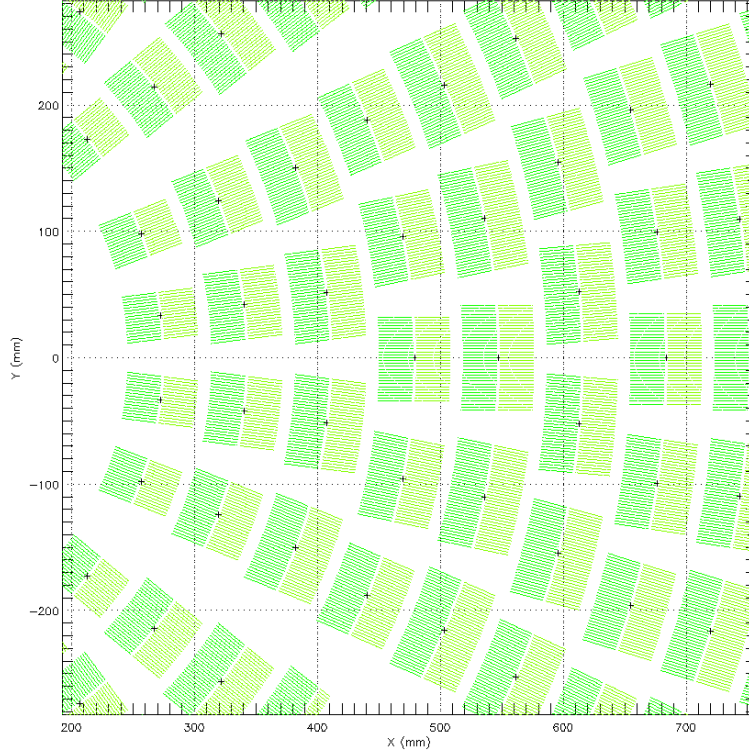


Figure 7. Locating the reflective pores in the ATHENA standard design. In this magnified view, each pore is represented as a dot, and the center of each MM is represented by a cross. The coordinates were used to carry out the computation examples in Sect. 4.

on condition that  $\beta_2 \geq 0$  and where, as usual, we have approximated  $\Phi \simeq \Sigma \simeq \alpha_0^0(1 - \xi_0)$ . Computation of Eq. (28) requires the knowledge of the  $\beta$ 's, which follow the relations:

$$\beta_1^{nm} = \theta \cos \varphi_{nm} + 2n\Delta\alpha_w - \alpha_0^n, \quad (29)$$

$$\beta_2^{nm} = \beta_0^n - 2n\Delta\alpha_w - \theta \cos \varphi_{nm}, \quad (30)$$

having denoted with  $\beta_0^n = 3\alpha_0^0 + 3n\Delta\alpha_R$ , which would be the slope of the  $n$ -th secondary plate in the +1/+3 configuration. In all the wedge configurations,  $\Delta\alpha_w$  is provided by Eq. (16).

### 3.3 Stray light restriction to the detector area

Summing Eqs. (21) and (28) over all the pores in ATHENA, clearly return the total stray light effective area as out of the mirror assembly. However, only a part of the stray rays will reach the area of the detector, e.g., the Wide Field Imager (WFI); the rest of the stray light is expected to be lost in space, or hit the supporting structures and so be absorbed. Therefore, in order to obtain a meaningful estimation of the stray light impact, we have to restrict the summations to the sole pores that reflect stray rays into the detector area. Keeping the source at infinite distance, we can perform such a selection noting that the impact point of a ray originated by a pore at the coordinates  $(R_0^n, \varphi_{nm})$  is given by the parametric equations (see<sup>14</sup> with some adaptation):

$$x_1(\varphi_{nm}) = [R_0^n - 2(\alpha_0^n - 2n\Delta\alpha_w)f] \cos \varphi_{nm} + \theta f \cos 2\varphi_{nm}, \quad (31)$$

$$y_1(\varphi_{nm}) = [R_0^n - 2(\alpha_0^n - 2n\Delta\alpha_w)f] \sin \varphi_{nm} + \theta f \sin 2\varphi_{nm}, \quad (32)$$

valid for SL1, and

$$x_2(\varphi_{nm}) = [R_0^n - 2(\beta_0^n - 2n\Delta\alpha_w)f] \cos \varphi_{nm} + \theta f \cos 2\varphi_{nm}, \quad (33)$$

$$y_2(\varphi_{nm}) = [R_0^n - 2(\beta_0^n - 2n\Delta\alpha_w)f] \sin \varphi_{nm} + \theta f \sin 2\varphi_{nm}, \quad (34)$$

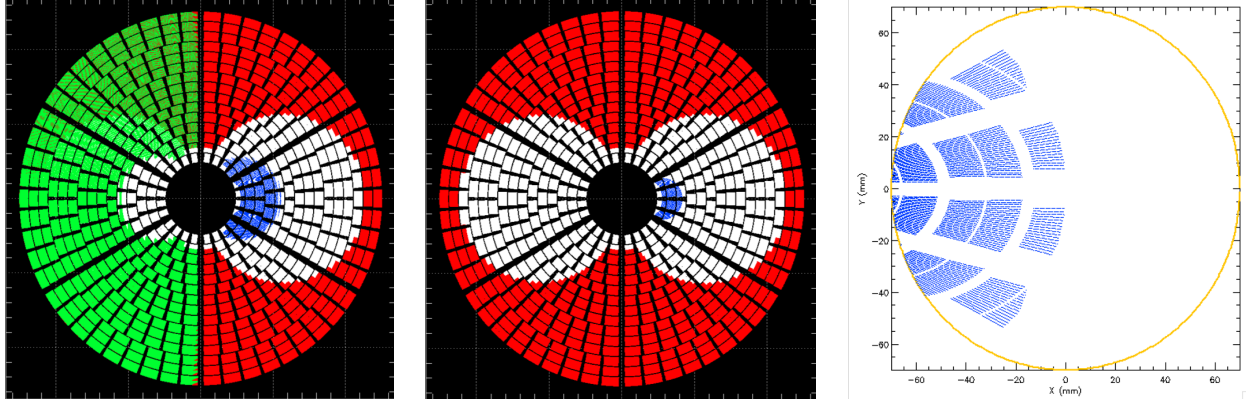


Figure 8. Point-like source, 40 arcmin off-axis,  $\varphi' = 0$  (i.e., on the right side, looking toward the focal plane). The aperture of the ATHENA mirror assembly was colored in red where pores contributed to the double reflection; the green color mark SL1, blue SL2. White means that the pores are totally obstructed. Left: all the rays, as out of the MA. Center: only the rays that have reached the WFI area. Right: geometric stray-light in the WFI area. This depiction is purely geometric and does not account for the coating reflectivity.

which hold for SL2. The different possible wedge configurations, clearly affecting the incidence angles and the exit direction of the rays, are expressed via the parameter  $\Delta\alpha_w$  (Eq. (16)). As we keep the detector centered on the optical axis of the MA, the selection of the pores that geometrically contribute to the stray light area is obtained restricting the sum to the indices that fulfill one of the following conditions:

$$x_1^2 + y_1^2 \leq \rho^2, \quad (35)$$

$$x_2^2 + y_2^2 \leq \rho^2, \quad (36)$$

where  $\rho$  is the radius of the detector (14 cm for the WFI).

#### 4. COMPUTATION EXAMPLES

We now provide some simple examples of computation for the stray light effective area for the ATHENA MA, always assuming a point-like source at infinite distance. A number of different computations can be made; here we just want to prove the potentiality of this method, which returns the effective area for SL1 and SL2 in *less than 1 minute*, just applying Eqs. (21) to all the pores fulfilling either Eq. (35), and Eq. (28) to all those fulfilling Eq. (36). All the routine was easily coded in an IDL program. Additionally, the 2R focused area was computed from Eq. (17) applied to all the  $nm$  indices and to all the mirror modules, because all the pores were supposed to geometrically contribute to the focused image within the detector field of view, regardless of the off-axis angle (for illustrative purposes, here we did not consider that the focus goes beyond the edge of the WFI when  $\theta > 20$  arcmin). As for the reflectivity computation, we assumed a standard Iridium (30 nm) + amorphous Carbon (10 nm) coating. The Carbon overcoating is present only from the 9-th row outwards. Prior to the computation, the mirror reflectivity was computed in a wide range of incidence angles (0 to 4.6 deg), and energies (0.1 to 12 keV), constructing in this way a lookup table for  $r_\lambda(\alpha)$  and  $r_\lambda(\beta)$ . All the polar coordinates of the pore centers in the MA were located from the reference design of ATHENA and saved to file (Fig. 7). The pores were assumed with fixed dimensions of  $w = 2.13$  mm and  $h = 0.665$  mm, and  $t = \tau = 0.17$  mm.

Running the computation program for  $\theta = 40$  arcmin, we obtain the results shown in Fig. 8, showing only the geometric obstructions and not accounting for the stray light suppression due to the increased incidence angle and the consequent reflectivity reduction. While a large fraction of pores (in red) contributes to the 2R effective area, all the pores on the opposite side to the source start to miss the 2nd reflection, giving rise to SL1 (in green). However, all this contribution falls short of reaching the WFI area. Another area (blue) generates a significant fraction of SL2, but only a small part contaminates the WFI. Increasing the off-axis angle to 90 arcmin, we obtain a more severe obstruction of pores (Fig. 9), causing most X-rays to be blocked in both double reflection

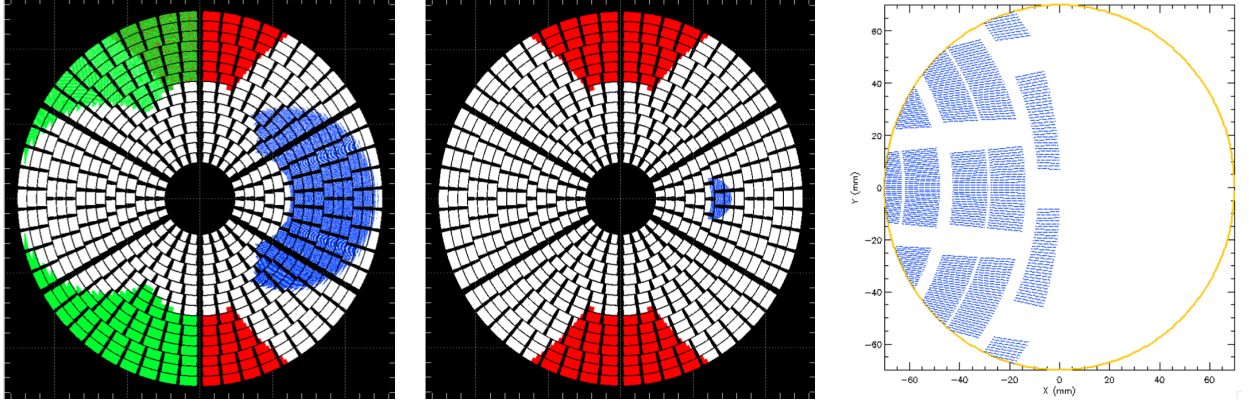


Figure 9. Point-like source, 90 arcmin off-axis (on the right side, looking toward the focal plane). Left: all the rays as out of the MA. Center: only the rays that have reached the WFI area. Right: geometric stray-light in the WFI area. The colors have the same meaning as in Fig. 8. In this case also, only a minor fraction from SL2 has reached the WFI area. The rendition just accounts for obstructions and is not weighted over the coating reflectivity.

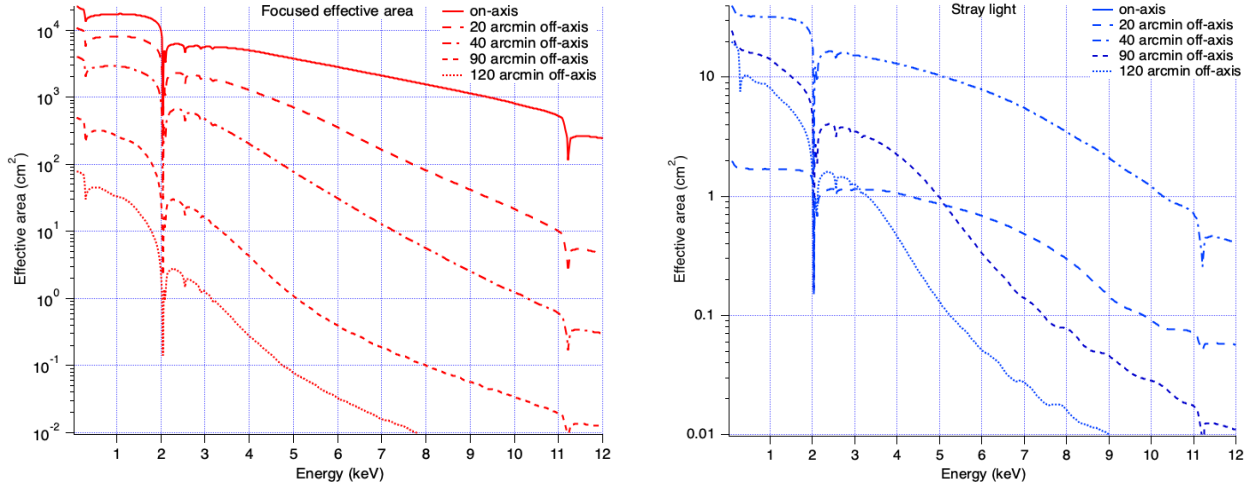


Figure 10. Left: computed effective area focused on the focal plane, as a function of the energy, for different off-axis angles. Right: computed effective area for stray light within the WFI area (kept aligned to the optical axis), as a function of the energy, for different off-axis angles.

and stray light. Once again, only a minority of stray rays succeeds at reaching the WFI area, and (with the exception of a minor contribution from SL1 at  $\theta < 20$  arcmin), it is entirely due to SL2.

Repeating the computation for a number of different  $\theta$  values, the effective area dependence on the energy can be explored for both focused and stray light effective area (Fig. 10). Exploring the dependence on the  $\varphi'$  polar angle of the source would also be possible, but its impact is expectedly much less pronounced.

## 5. CONCLUSIONS AND FUTURE WORK

In this paper, we have laid the foundations for a fully-analytical treatment of stray light in an optical assembly based on the technology of pore optics, such as ATHENA. We have developed an analytical set of formulae to express the contribution of a single pore to the focused effective area, to the stray light due to single reflection on either the primary or the secondary mirrors. The effective area of a pore can be expressed as an analytical function of its dimensions and the incidence angles, which in turn vary with the radius, the focal length, and the wedge configuration. Even though each SPO MM is based on the Wolter-I geometry (while the individual modules follow a WS arrangement in the full MA), the formalism can be easily generalized to a possible WS geometry within each mirror module, just modifying the vignetting coefficients that express the obstruction of

the focused or the stray light. These modified coefficients were also derived and presented in this paper. Despite some simplification (double-cone approximation, non-reflective ribs/membranes, ...) the approach based on the analytical calculation has allowed us to estimate the stray light impact for ATHENA in a few minutes. The fast computation can provide a useful feedback in the design of a hypothetical pre-collimator for ATHENA, and in order to assess the benefits versus possible risks coming from misalignments of structures to grids, e.g., during the launch.

In a forthcoming development of this work, we foresee a detailed comparison of the outcome with the findings of the detailed ray-tracing in order to validate both methods and so determine the level of accuracy in the effective area predictions. A possible extension of the mathematical treatment to include a small reflectivity from pore walls is also envisaged.

## APPENDIX A. DERIVATION OF TANGENTIAL VIGNETTING COEFFICIENTS

In this section, we briefly derive the expressions of the tangential vignetting coefficients (Fig. 6) for two adjacent mirror pairs, in double cone approximation. These results are directly applicable to pore optics even if, for generality, we assume a non-negative shift  $\Delta z$  between the intersection planes of the two pairs along the optical axis. We adopt the symbols explained in Fig. 5, omit the  $nm$  pore indices, and simplify the derivation recalling two facts already proven:<sup>13</sup>

- consecutive ray reflections on the two mirror segments, to very good approximation, occur at the same polar angle  $\varphi$ . Therefore, as far as the tangential vignetting is concerned, we restrict the computation into the incidence plane;
- the vignetting coefficients depend on  $\varphi$ , only via Eqs. (1),(2), (3), which provide the incidence angles  $\alpha_1$ ,  $\alpha_2$ , and  $\beta_2$ .

Clearly, the double-reflection vignetting involves only the reflective pair and so remains unchanged:  $V = L_2\alpha_2/L_1\alpha_1$  (Eq. (5)). For the others, we follow the passages described in a previous paper,<sup>14</sup> always assuming the angles shallow enough to approximate the goniometric functions with their arguments.

### A.1 Tangential vignetting: double reflection

We start from the vignetting at the entrance pupil (Fig. 6, A). A ray passing by the outer edge of the obstructing pair at its maximum radius intersects the primary segment of the reflecting pair (Fig. 11, left, ray (1)) at  $z = Z_1$ ,  $r = R_0 + Z_1\alpha_0$ . If the incidence angle on the primary mirror is  $\alpha_1$ , then the ray forms with the  $z$ -axis an angle  $\alpha_1 - \alpha_0$ , and the ray slope is  $-1/(\alpha_1 - \alpha_0)$ . Therefore, the ray equation in the incidence plane is

$$\frac{z - Z_1}{r - (R_0 + \alpha_0 Z_1)} = -\frac{1}{\alpha_1 - \alpha_0}. \quad (37)$$

Now, enforcing the condition that the ray passes by the upper edge of the obstructing pair, at the coordinates  $r = R_M^*$ ,  $z = L_1^* + \Delta z$ , and solving for  $Z_1$ , we obtain:

$$Z_1 = (L_1^* + \Delta z) - \frac{\Phi L_1^* + \alpha_0 \Delta z}{\alpha_1}, \quad (38)$$

where we have used the  $\Phi$  definition, Eq. (4). The  $Z_1$  coordinate corresponds to the upper edge of the shadow cast by the obstructing pair; hence, the unobstructed mirror length fraction is  $V_1 = (L_1 - Z_1)/L_1$ :

$$V_1 = 1 + \frac{L_1^*(\Phi - \alpha_1) + \Delta z(\alpha_0 - \alpha_1)}{L_1\alpha_1}. \quad (39)$$

The coefficient  $V_2$  that describes the obstruction at the intersection plane is derived in a totally similar way (Fig. 11, left, ray (2)). After the first reflection, rays forms an angle  $\alpha_1 + \alpha_0$  with the  $z$ -axis. We consider the reflected ray coming from the generic point of the primary mirror at  $(R_0 + \alpha_0 Z_2, Z_2)$ :

$$\frac{z - Z_2}{r - (R_0 + \alpha_0 Z_2)} = \frac{1}{\alpha_1 + \alpha_0}. \quad (40)$$



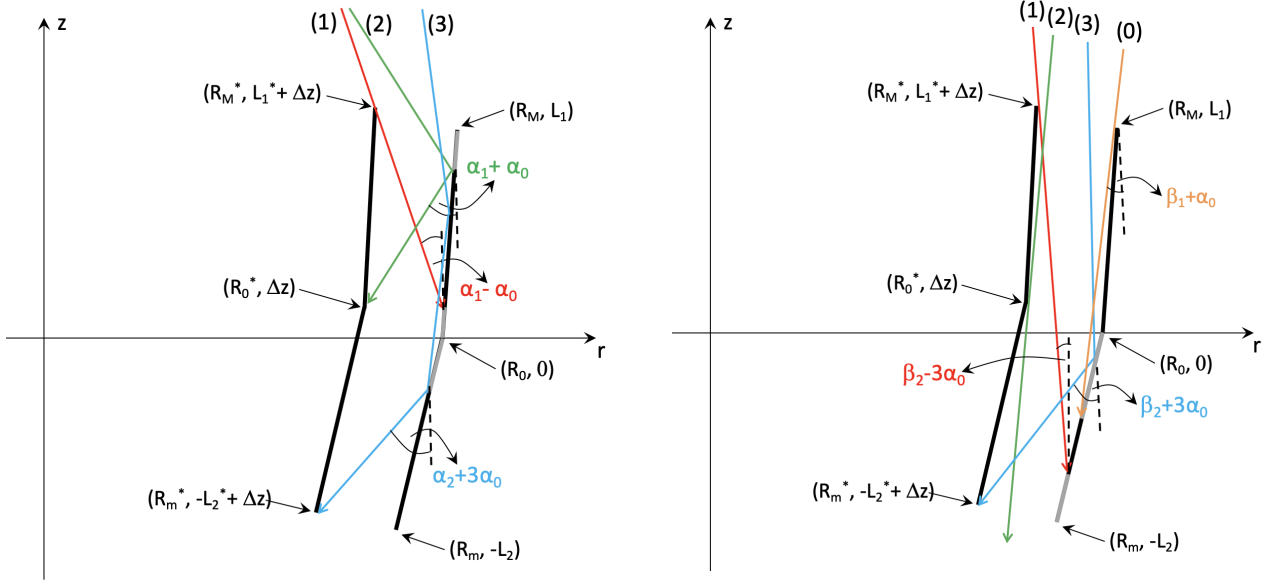


Figure 11. Left: obstruction of doubly-reflected rays. Right: obstruction of secondary stray light. The shaded regions are grayed. For 2R: (1) before reflections, at the entrance pupil; (2) after first reflection, on the primary segment of the obstructing pair; (3) after two reflections, on the secondary segment of the obstructing pair. For SL2: (0) shadow cast by the primary mirror of the *reflective* pair; (1) shadow cast by the primary mirror of the *obstructing* pair; (2) shadow cast by the secondary mirror of the obstructing pair (intersection not shown); (3) after reflection, on the backside of the secondary mirror of the obstructing pair. The mirror spacing was greatly exaggerated.

Imposing the condition that the last obstructed ray passes by  $(R_0^*, +\Delta z)$ , and using the definition of  $\Psi$  (Eq. (4)), we can derive  $Z_2$ ,

$$Z_2 = \frac{L_1 \Psi + \Delta z (\alpha_1 + \alpha_0)}{\alpha_1}, \quad (41)$$

and, since the shaded length is located at axial coordinates  $z > Z_2$ , provided that it is non-negative, the second vignetting coefficient is  $V_2 = Z_2/L_1$ , i.e.,

$$V_2 = \frac{L_1 \Psi + \Delta z (\alpha_1 + \alpha_0)}{L_1 \alpha_1}. \quad (42)$$

Regarding the vignetting at the exit pupil, a generic ray after the second reflection forms an angle  $\alpha_2 + 3\alpha_0$  with the  $z$ -axis and is originated at the generic axial coordinate  $Z_3$  of the secondary mirror (Fig. 11, left, ray (3)). This returns the reflected ray equation:

$$\frac{z - Z_3}{r - (R_0 + 3\alpha_0 Z_3)} = \frac{1}{\alpha_2 + 3\alpha_0}. \quad (43)$$

Fulfilling now the condition that the last obstructed ray passes through the point  $(R_m^*, -L_2^* + \Delta z)$ , and introducing the definition of  $\Sigma$  (Eq. (4)), we easily derive  $Z_3$ :

$$Z_3 = \frac{L_2^* (\Sigma - \alpha_2) + \Delta z (\alpha_2 + 3\alpha_0)}{\alpha_2}. \quad (44)$$

The secondary mirror length at  $z > Z_3$  is obstructed and covers a length  $-Z_3$ . Using the expression of  $V$  (Eq. (5)), we see that the rays coming from the shaded length are the ones reflected on the primary segment at  $z < Z'_3 = -Z_3 \alpha_2 / \alpha_1$ . The resulting vignetting coefficient is  $V_3 = 1 - Z'_3 / L_1$ , or

$$V_3 = 1 + \frac{L_2^* (\Sigma - \alpha_2) + \Delta z (\alpha_2 + 3\alpha_0)}{L_1 \alpha_1}. \quad (45)$$

We finally note that Eqs. (39), (42), and (45) correctly reduce to the usual expressions<sup>14</sup> when  $\Delta z = 0$ .

## A.2 Tangential vignetting: primary stray light

As for primary stray light, (Fig. 6, B), the first two types of obstructions remain unchanged. Consequently, the expressions for  $V_1$  and  $V_2$  (Eqs. (39) and (42)) are also valid for the SL1 obstruction. The last source of obstruction for SL1 is totally analogous to the third one described in Sect. A.1, with the only difference that the ray did not make the second reflection. Hence, we just use Eq. (40), this time enforcing the intersection at the point  $(R_m^*, -L_2^* + \Delta z)$ , and recalling the  $\Sigma$  definition (Eq. 4). Solving for  $Z_2$ , we find

$$Z_2 = \frac{L_2^*(\Sigma + 2\alpha_0 - \alpha_1) + \Delta z(\alpha_1 + \alpha_0)}{\alpha_1}. \quad (46)$$

Now, since this obstruction affects the mirror area near the entrance of the primary mirror, the related vignetting coefficient is  $V_3 = Z_2/L_1$ , i.e., recalling that  $\alpha_1 + \alpha_2 = 2\alpha_0$ ,

$$V_3 = \frac{L_2^*(\Sigma + \alpha_2) + \Delta z(\alpha_1 + \alpha_0)}{L_1\alpha_1}. \quad (47)$$

When  $\Delta z = 0$ , this expression becomes the one already shown in a previous contribution.<sup>15</sup>

## A.3 Tangential vignetting: secondary stray light

We now consider the direct incidence on the secondary mirror surface with slope  $3\alpha_0$  and its possible obstructions (Fig. 6, C). There is no second reflection in this case, therefore the double-reflection vignetting coefficient  $V$  (Eq. 5) cannot be used. However, the primary segment of the reflective plate pair could cast a shadow on the secondary one, and this is an additional source of vignetting, which we characterize via another coefficient that we keep denoting with  $V$ . We can easily find the related expression by noting that (Fig. 11, right, ray (0)) the ray passing by the upper edge of the reflective pair, and forming an angle  $\beta_1 + \alpha_0$  with the  $z$ -axis, has the analytical expression

$$\frac{z - L_1}{r - R_M} = \frac{1}{\beta_1 + \alpha_0}, \quad (48)$$

where  $\beta_1 = -\alpha_1$  is positive *only if* the primary segment does cast a shadow onto the secondary one. Finding now the intersection with the secondary surface of equation  $r = R_0 + 3\alpha_0 z$ , considering that  $\beta_1 + \beta_2 = 2\alpha_0$  and  $R_M = R_0 + \alpha_0 L_1$ , we obtain the solution at

$$Z_0 = -\frac{L_1\beta_1}{\beta_2}, \quad (49)$$

and since the unobstructed part lies at  $z < Z_0$ , the vignetting coefficient  $V = (L_2 - Z_0)/L_2$  reads

$$V = 1 - \frac{L_1\beta_1}{L_2\beta_2}. \quad (50)$$

The choice of dubbing this coefficient with  $V$  appears thereby justified by the dependence on the incidence angles, which is totally similar to that of Eq. (5).

As it now comes to the obstruction by the inner mirror pair, the first source of obscuration is represented by the upper edge with coordinates  $(R_M^*, L_1^* + \Delta z)$ . A ray passing through that point and having slope:  $-1/(\beta_2 - 3\alpha_0)$ , is traced by the equation

$$\frac{z - L_1^* - \Delta z}{r - R_M^*} = \frac{1}{3\alpha_0 - \beta_2}, \quad (51)$$

(see Fig. 11, right, ray (1)) and if we find its intersection with the secondary surface at  $(R_0 + 3\alpha_0 Z_1, Z_1)$ , we obtain, using the definition of  $\Phi$  (Eq. (4)):

$$Z_1 = -\frac{L_1^*(\Phi + 2\alpha_0 - \beta_2) + \Delta z(3\alpha_0 - \beta_2)}{\beta_2}. \quad (52)$$

The unobscured fraction of the secondary mirror length is  $V_1 = -Z_1/L_2$ , or, using the identity  $3\alpha_0 - \beta_2 = \alpha_0 - \alpha_1$ ,

$$V_1 = \frac{L_1^*(\Phi - \alpha_1) + \Delta z(\alpha_0 - \alpha_1)}{L_2\beta_2}. \quad (53)$$

The second vignetting coefficient can be computed in a totally similar way: this time, the ray of interest is (2) in Fig. 11, right, whose equation is

$$\frac{z - \Delta z}{r - R_0^*} = \frac{1}{3\alpha_0 - \beta_2}. \quad (54)$$

Enforcing the intersection with the secondary surface at  $(R_0 + 3\alpha_0 Z_2, Z_2)$ , we derive  $Z_2$ ,

$$Z_2 = -\frac{L_1\Psi + \Delta z(3\alpha_0 - \beta_2)}{\beta_2}, \quad (55)$$

which, when substituted into  $V_2 = -Z_2/L_2$ , yields

$$V_2 = \frac{L_1\Psi + \Delta z(\alpha_0 - \alpha_1)}{L_2\beta_2}, \quad (56)$$

where we made use of the  $\Psi$  definition (Eq. (4)).

The third vignetting coefficient is obtained by having a ray ((3) in Fig. 11, right) originate from the generic reflection point  $(R_0 + 3\alpha_0 Z_3, Z_3)$  and form an angle  $\beta_2 + 3\alpha_0$  with the optical axis,

$$\frac{z - Z_3}{r - (R_0 + 3\alpha_0 Z_3)} = \frac{1}{\beta_2 + 3\alpha_0}, \quad (57)$$

and enforcing the condition that the ray intersects the lower edge of the obstructing pair,  $(R_m^*, -L_2^* + \Delta z)$ ,

$$Z_3 = \frac{L_2^*(\Sigma - \beta_2) + \Delta z(\beta_2 + 3\alpha_0)}{\beta_2}, \quad (58)$$

where we tused the  $\Sigma$  definition (Eq. (4)). Obstruction occurs if  $Z_3 < 0$ , i.e., only if this coordinate is within the physical length of the secondary mirror. If so, the unobstructed fraction of the secondary mirror is  $V_3 = (L_2 + Z_3)/L_2$ , yielding

$$V_3 = 1 + \frac{L_2^*(\Sigma - \beta_2) + \Delta z(\beta_2 + 3\alpha_0)}{L_2\beta_2}. \quad (59)$$

Taking  $\Delta z = 0$ , we reduce  $V_1$ ,  $V_2$ , and  $V_3$  to their usual form.<sup>15</sup>

## ACKNOWLEDGMENTS

The ‘‘Silicon Pore Optics SImUlation and Modelling’’ project (SImPOSIUM) is supported by the European Space Agency (contract number 4000114410).

## REFERENCES

- [1] Bavdaz, M., Wille, E., Ayre, M., Ferreira, I., Shortt, B., Fransen, S., Millinger, M., Collon, M., Vacanti, G., Barrière, N., Landgraf, B., et al., ‘‘ATHENA optics technology development,’’ Proc. SPIE 12181, this conference
- [2] Collon M. J., Abalo, L., Babic, L., Barrière, N. M., Bayerie, A., Castiglione, L., Eenkhoorn, N., Girou, D., Günther, R., Hauser, E., et al., ‘‘The development of the mirror for the Athena X-ray mission,’’ Proc. SPIE 12181, this conference
- [3] Van Speybroeck, L., Chase, R., ‘‘Design parameters of paraboloid-hyperboloid telescopes for X-ray astronomy,’’ Appl. Opt. 11(2), 440 (1972)

- [4] Willingale, R., Spaan, R., "Improving the angular resolution of the conical Wolter-I silicon pore optics (SPO) mirror design for the International X-ray Observatory (IXO)," Proc. SPIE 7732, 773241 (2010)
- [5] Wille, E., Bavdaz, M., Oosterbroek, T., et al., "Silicon Pore Optics Mirror Modules for Inner and Outer Radii," Proc. SPIE 9603, 96030L (2015)
- [6] Handick, E., Cibik, L. Krumrey, M., "Upgrade of the X-ray parallel beam facility XPBF 2.0 for characterization of silicon pore optics," Proc. SPIE 11444, 114444G (2020)
- [7] Salmaso, B., Basso, S., Ghigo, M., Spiga, D., Vecchi, G., Sironi, G., Cotroneo, V., Conconi, P., Redaelli, E., Bianco, A., Pareschi, G., Tagliaferri, G., Sisana, D., et al., "X-ray tests of the ATHENA mirror modules in BEaTriX: from design to reality," Proc. SPIE 12181, this conference
- [8] Valsecchi, G., Vernani, D., Marioni, F., Zocchi, F., Bianucci, G., "Alignment and integration of the SPO mirror modules onto the ATHENA telescope," Proc. SPIE 12181, this conference
- [9] Chase, R., Van Speybroeck, L., "Wolter-Schwarzschild Telescopes for X-Ray Astronomy," Appl. Opt. 12(5), 1042 (1973)
- [10] Friedrich, P., Rohé, C., Gaida, R., Hartwig, J., Soller, F., Bräuninger, H., Budau, B., Burkert, W., Burwitz, V., J. Eder, G. Hartner, B. Menz, P. Predehl, "The eROSITA x-ray baffle," Proc. SPIE 9144, 91444R (2014)
- [11] Della Monica Ferreira, D., Bergbäck Knudsen, E., Westergaard, N.J., Christensen, F.E., et al., "Simulating X-ray telescopes with McXtrace: a case study of ATHENA's optics," Proc. SPIE 9905, 990575 (2016)
- [12] Willingale, R., "Stray x-ray flux in the Athena Mirror," Proc. SPIE 11119, 111190Q (2019)
- [13] Spiga, D., Cotroneo, V., Basso, S., Conconi, P., "Analytical computation of the off-axis effective area of grazing incidence X-ray mirrors," A&A 505(1), 373 (2009)
- [14] Spiga, D., "Optics for X-ray telescopes: analytical treatment of the off-axis effective area of mirrors in optical modules," A&A 529, A18 (2011)
- [15] Spiga, D., "Analytical computation of stray light in nested mirror modules for X-ray telescopes," Proc. SPIE 9603, 96030H (2015)
- [16] Spiga, D., "X-ray mirror module analytical design from field of view requirement and stray light tolerances," Proc. SPIE 9905, 99056Q (2016)
- [17] Spiga, D., Christensen, F. E., Bavdaz, M., Civitani, M. M., Conconi, P., Della Monica Ferreira, D., Bergbäck Knudsen, E., Massahi, S., Pareschi, G., Salmaso, B., Shortt, B., Tayabaly, K., Westergaard, N. J., Wille, E., "Simulation and modeling of silicon pore optics for the ATHENA X-ray telescope," Proc. SPIE 9905, 99055O (2016)
- [18] Spiga, D., Della Monica Ferreira, D., Shortt, B., Bavdaz, M., Bergback Knudsen, E., Bianucci, G., Christensen, F., Civitani, M., Collon, M., Conconi, P., Fransen, S., Marioni, F., Massahi, S., Pareschi, G., Salmaso, B., Jegers, A. S., Tayabaly, K., Valsecchi, G., Westergaard, N., Wille, E., "Optical simulations for design, alignment, and performance prediction of silicon pore optics for the ATHENA X-ray telescope," Proc. SPIE 10399, 103990H (2017)
- [19] Spiga, D., "Effective area analytical computation for segmented optics," INAF/OAB int. rep. 16/2014 (2014)